

1 **Detailed assessment of low-voltage zones localization by**
2 **cardiac MRI in patients with implantable devices**

**Running Title: Optimization strategies for scar localization using CMR in
patients with ICDs**

Michele Orini PhD* ^{1,2}, Andreas Seraphim MBBS* ^{1,3}, Adam Graham PhD ², Anish Bhuva PhD^{1,3}, Ernesto Zacur PhD ⁴, Peter Kellman PhD⁵, Richard Schilling MD MRCP FHRs ², Ross Hunter PhD, MRCP FHRs², Mehul Dhinoja MRCP FHRs ², Malcolm C. Finlay PhD², Syed Ahsan MD FRCP ², Anthony W. Chow MD MRCP FHRs ², James C. Moon MD ^{1,3}, Pier D. Lambiase PhD FRCP FHRs^{# 1,2}, Charlotte Manisty PhD^{# 1,3}

* Joint first authors, # Joint senior Authors

1: Institute of Cardiovascular Science, University College London, UK

2: Department of Cardiac Electrophysiology, Barts Heart Centre, Barts Health NHS Trust, London, United Kingdom

3: Department of Cardiovascular Imaging, Barts Heart Centre, Barts Health NHS Trust, London, United Kingdom

4: Department of Biomedical Engineering, University of Oxford, Oxford, UK.

5: National Institutes of Health, Bethesda, USA

Corresponding authors:

- Prof Pier D. Lambiase, Institute of Cardiovascular Science, 5 University St, London WC1E 6JF, Email: p.lambiase@ucl.ac.uk, +44(0)203 679 4407
- Dr Charlotte H. Manisty, Department of Cardiac Imaging, Barts Heart Centre, W Smithfield, London EC1A 7BE. Email: c.manisty@ucl.ac.uk

3 **Sources of Funding**

4 AB and AS are supported by doctoral research fellowships from the British Heart
5 Foundation (FS/16/46/32187 and FS/18/83/34025). JCM, PDL, MO and CM are
6 directly and indirectly supported by the University College London Hospitals and

7 Barts Hospital NIHR Biomedical Research Centres. PL has received research grants
8 from Boston Scientific, Medtronic and Abbott and speaker fees from Medtronic.

Abstract

Aims: Scar evaluation by late gadolinium enhancement cardiac magnetic resonance (LGE-CMR) can assist ventricular tachycardia (VT) ablation, but challenges with electro-anatomical maps (EAMs) co-registration and presence of imaging artefact from cardiac implantable electronic devices (CIED) limit accuracy. We assessed the performance and limitations of low-voltage zones (LVZ) localization by optimised LGE-CMR scar imaging in patients with CIEDs.

Methods: 10 patients underwent VT ablation and pre-procedural LGE-CMR using wideband imaging. Scar was segmented from CMR pixel signal intensity (PSI) maps using commercial software (ADAS) with bespoke tools and compared to detailed EAMs (CARTO). Co-registration of EP and imaging derived scar was performed using the aorta as a fiducial marker and the impact of co-registration was determined by assessing intra/inter-observer variability and using computer simulations. Spatial smoothing was applied to assess correlation at different spatial resolutions and to reduce noise.

Results: PSI maps localized low-voltage zones ($V < 1.5$ mV) with area under the ROC curve $AUC = 0.82$ (0.76–0.83), sensitivity=74% (71%–77%) and specificity=78% (73%–83%) and correlated with bipolar voltage, $r = -0.57$ (-0.68 – -0.42) across patients. In simulations, small random shifts and rotations worsened LVZ localization in at least some cases. The use of the full aortic geometry ensured high reproducibility of LVZ localization ($r > 0.86$ for AUC). Spatial smoothing improved localization of LVZ. Results for LVZ with $V < 0.5$ mV were similar.

Conclusion: In patients with CIEDs, novel wideband CMR sequences and personalised co-registration strategies can localize LVZ with good accuracy and may assist VT ablation procedures.

9 **Keywords:** Cardiac mapping, Cardiovascular MRI, Scar, Ventricular tachycardia,
10 Ablations

11 **Condensed Abstract**

12 Cardiac magnetic resonance (CMR) imaging has the potential to localize scar non-
13 invasively and improve ventricular tachycardia (VT) ablation. However, artefacts due
14 to implantable devices (CIEDs), inaccuracy in co-registration with electro-anatomical
15 maps and noise may limit its use. We used optimized wideband sequences and
16 image analysis to assess performance and limitations of low-voltage zones (LVZ)
17 localization by CMR in patients with CIEDs. We found that using the thoracic aorta
18 for co-registration provides good point-by-point correlation ($r \sim -0.60$) and good LVZ
19 discrimination ($AUC \sim 0.80$), with high intra- and inter-observer reproducibility. Spatial
20 smoothing improved overall CMR-EAM agreement at the expense of reducing spatial
21 resolution.

22

Abbreviations

VT: Ventricular Tachycardia

EAM: Electro-anatomical mapping

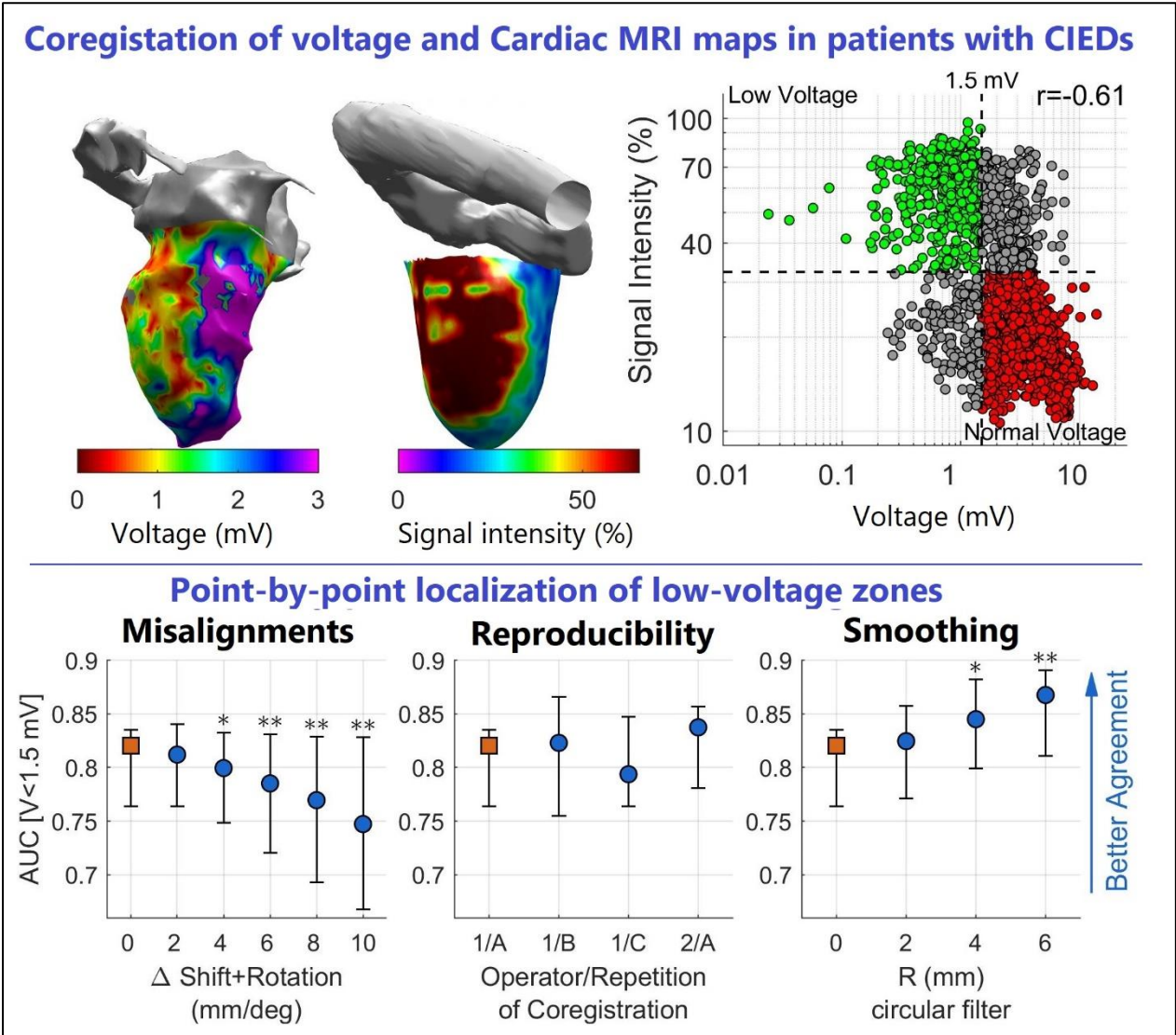
LGE-CMR: Late Gadolinium enhanced Cardiac Magnetic Resonance

CIED: Cardiac Implantable Electronic Device

LVZ: Low-voltage Zone

PSI: Pixel Signal Intensity

23 **Central Figure**



24
25

26 Introduction

27 Catheter ablation improves outcomes in patients with frequent life-threatening
28 ventricular tachycardia (VT). However, VT recurrence rates remain unacceptably
29 high necessitating the pursuit of more effective ablation strategies (1). Late
30 gadolinium enhancement cardiac magnetic resonance (LGE-CMR) can provide non-
31 invasive visualisation of arrhythmogenic substrate (2–6) and its integration with
32 electro-anatomical mapping (EAM) can improve procedural outcomes (7–9). Indeed,
33 recent work has proposed the utilisation of an MRI-guided approach (9), based on
34 EAM system and CMR-derived scar co-registration. The integration of LGE-CMR
35 scar maps and EAM for VT ablation is however not widespread. There are several
36 reasons for this. Firstly, the precise co-registration of whole heart LGE-CMR with
37 EAM is challenging. Secondly, most patients requiring VT ablation have cardiac
38 implantable electronic devices (CIEDs) in-situ. Although scanning can now be
39 performed safely with appropriate protocols (10,11), meaning almost all patients
40 could now have LGE-CMR, the CIED itself generates image artefact (signal dropout,
41 hyperintensity artefact) that hinders scar delineation. Dedicated sequences
42 incorporating a wideband inversion pulse can reduce this (10), but few studies have
43 examined feasibility of LGE-CMR and EAM co-registration in these patients (8,12,13)
44 and the agreement in scar localization between the two modalities remains
45 undetermined. In this study, we deploy a novel wideband LGE sequence that is fast,
46 free-breathing and incorporates phase-sensitive inversion recovery (10). We
47 investigate the spatial correlation between low-voltage zones from state of the art
48 EAM and 3D CMR pixel signal intensity (PSI) maps in patients with CIEDs (10) and
49 focused on optimal approaches for co-registration that maximise clinical utility.

50 **Methods**

51 **Study population**

52 The study was approved by the National Health Service Research Ethics Committee
53 (14/LO/0360) and Health Research Authority (HRA) and was conducted in
54 accordance with the Declaration of Helsinki. All subjects provided written, informed
55 consent. Ten (n=10) consecutive patients (1 female, median age 75 years,
56 interquartile range 70 – 79 years, 9 ischemic cardiomyopathy, 1 non-ischaemic
57 dilated cardiomyopathy) with CIEDs (5 ICD, 5 CRT-D, 50% non-MR conditional)
58 undergoing catheter VT ablation between 2017 and 2019 (8 first time, 2 repeat
59 ablations, Table 1) were included in the analysis. Specifically, patients were included
60 if they underwent LGE-CMR shortly before catheter ablation and if a detailed LV
61 substrate map and a complete aortic geometry, including ascending, arch and
62 descending aorta, were collected during the electrophysiological study. In all
63 patients, catheter ablation was performed because of recurrent VTs and frequent
64 ICD therapy. Five cases were elective and 5 were urgent cases for treatment of
65 incessant VT or VT storm. Among the 9 patients with ischaemic cardiomyopathy,
66 myocardial infarction was more frequently seen in the anterior wall (bullseye plot of
67 scar distribution is shown in the Supplementary Material, Figure S1).

68 **CMR protocol and data analysis**

69 All patients underwent LGE-CMR prior to their procedure. CMR studies were
70 performed on a 1.5T scanner (Aera, Siemens Healthineers, Erlangen, Germany)
71 using a 30-channel phased array receiver coil, scanned at Normal Operating Mode
72 (SAR limit <2 W/kg). In brief, device interrogation and re-programming occurred
73 immediately before and after scanning, according to international guidelines.

74 Patients were monitored throughout using ECG and pulse oximetry waveform
75 assessment.

76 An axial stack of images through the thorax was acquired for visualisation of
77 extracardiac structures, including the thoracic ascending and descending aorta to
78 enable co-registration with EAM data. This used a black blood Half-Fourier
79 Acquisition Single-shot Turbo spin Echo (HASTE) sequence, with 5mm slice
80 thickness and zero gap between slices. Late gadolinium images were acquired 10-
81 15 min after administration of 0.1 mmol/kg of Dotarem (Guerbet S.A.,Paris). The
82 sequence used was a 2D motion-corrected (free-breathing) single-shot FLASH
83 sequence with a 3.9 kHz (wideband) inversion pulse, with flip angle of 10°, phase
84 sensitive inversion recovery (PSIR)(10) and 24 averages to recover signal to noise.
85 Contiguous 4 mm short-axis slices were acquired with spatial resolution of 1.9x1.4
86 mm, which was interpolated to 1.4x1.4 mm for display and analysis. Epicardial and
87 endocardial borders were segmented, generating a 3D pixel signal intensity map of
88 the left ventricle (LV) using custom software (ADAS-VT, Galgo Medical, Spain) (6–8)
89 . Nine concentric surface layers from sub-endocardium (10% of wall thickness) to
90 sub-epicardium (90% of wall thickness) were created automatically. Subsequently,
91 pixel signal intensity (PSI) maps were projected over each LV layer using a trilinear
92 interpolation and color-coding to visualize PSI distribution. PSI was normalized, with
93 global minimum and maximum across all layers set equal to 0 and 100, respectively.
94 A tool in the same software was also used to create a 3D surface representation of
95 the aorta from the 2D axial anatomical images and to co-register this with the LV PSI
96 map.

97 EAM protocol and data analysis

98 Procedures were performed under conscious sedation using diamorphine and
99 midazolam, or general anaesthetic. Vascular access was obtained under ultrasound
100 guidance using Seldinger technique via the right femoral vein and/or right femoral
101 artery. The LV was accessed retrogradely via the aorta in all cases. Trans-septal
102 puncture was additionally performed in 4 cases to gain better overall access and
103 mapping coverage of the LV. A full geometry of the ascending, arch, and descending
104 aorta was created for co-registration with CMR-LGE scar meshes. Collection of this
105 geometry took less than 5 minutes in each case. A voltage map was created using a
106 multipolar catheter (Pentaray, CARTO, Biosense-Webster, CA), and the ST SF
107 Thermocool ablation catheter was also used in some cases. Most of intracardiac
108 mapping was performed continuously with criteria for collecting data including close
109 tissue proximity (using Tissue Proximity Indicator for Pentaray), position stability and
110 contact force within 2-40 g (when using the ablation catheter). Occasionally, data
111 collection was performed manually. EAM generated using less than 100 electrode
112 points were excluded.

113 CARTO generated meshes describing the spatial distribution of bipolar voltage of the
114 LV endocardium were exported for off-line analysis. Bipolar voltage <1.5 mV and
115 <0.5 mV was considered indicative of scar and dense scar, respectively.

116 EAM-CMR comparison

117 PSI color-coded maps were not visible to operators during the electrophysiological
118 study to reduce potential biases and co-registration of EAM and CMR geometries
119 was performed retrospectively (after each case) using bespoke software (Matlab,
120 The Mathworks, Inc, MA) (14,15) that allows the operator to move and rotate EAM
121 and CMR geometries and inspect the alignment under any viewpoint ([Video 1](#) in

122 Supplementary Material). Co-registration was manually performed and visually
123 determined by an expert independent of subsequent analysis and blinded to color-
124 coded maps of voltage and PSI (i.e. solely based on anatomical information).
125 Emphasis was placed on the simultaneous alignment of the ascending, arch and
126 descending aorta, and the LV apex. No other extra-cardiac structure was
127 systematically utilised. After co-registration, each vertex belonging to the EAM
128 geometry (i.e. the triangular mesh produced during cardiac mapping) was paired to
129 the closest vertex of the PSI map, provided that the Euclidean distance (D) between
130 them was $D \leq 8$ mm.

131 The impact of EAM-CMR co-registration on the localization of low-voltage zones was
132 assessed by reproducibility analysis and simulations. Intra- and inter-observer
133 reproducibility was assessed by repeating co-registration twice (same operator, with
134 more than 48 hours between repetitions) and by a second expert operator,
135 respectively. Repeated co-registrations were compared by measuring the difference
136 between the location of the aligned geometries as shifts and rotations (Euler's rule)
137 along and about the XYZ axes. The simulation study was carried out as follows. After
138 co-registration, small shifts and rotations were algorithmically applied to the EAM
139 and low-voltage zones localization re-assessed. In total, the analysis was repeated
140 320 times per case, consistent with configurations obtained by applying
141 simultaneous shifts and rotations of $\pm\Delta X$ mm and $\pm\Delta X^\circ$ along and around the 3
142 major axes ($2^6=64$ configurations), where $\Delta X = 2^\circ, 4^\circ, 6^\circ, 8^\circ$ and 10° . [Video 3](#) in
143 Supplementary Material shows the effect of shifts and rotations of up to ± 10 mm and
144 $\pm 10^\circ$ on one representative EAM.

145 As the agreement between voltage and PSI is thought to be affected by each
146 modality's spatial resolution and noise, we sought to modulate spatial resolution and

147 reduce noise by implementing spatial smoothing. This assigns to each point in a map
148 the average value of its neighbouring points within a given radius. Systematic
149 variation of this radius (circular linear filters with radius equal to 2, 4 and 6 mm)
150 allowed evaluation of the impact of spatial resolution/noise reduction on agreement
151 between EAM voltage and PSI. [Video 2](#) in Supplementary Material shows the effect
152 of increasing spatial smoothing on representative voltage and PSI maps.

153 **Statistical analysis**

154 Data distribution is reported as median, 1st – 3rd quartile. Correlation was assessed
155 using the Spearman's correlation coefficient (r). Assessment of binary classification
156 of low-voltage zones characterized by $V < 0.5$ mV or $V < 1.5$ mV was performed using
157 ROC curves. The area under the ROC curve (AUC) as well as sensitivity and
158 specificity obtained using the optimum PSI threshold (threshold corresponding to the
159 point closest to 100 sensitivity and specificity) were estimated for each case.
160 Sensitivity and specificity were then assessed using a fixed PSI threshold equal to
161 the median value of case-specific PSI thresholds. EAM for which the prevalence of
162 low-voltage zones was $< 3\%$ were not considered. Reported results represent
163 averaged values across CMR layers spanning from sub-endocardium (layer 10%) to
164 mid-myocardium (layer 50%) included. Results for each layer are reported in
165 Supplementary Material.

166 **Results**

167 CMR scans were performed without complication in all subjects, with no significant
168 changes in device parameters (battery voltage or lead sensitivities, thresholds or
169 impedances) between pre- and post-CMR device interrogations. PSI scar maps were
170 free from artefact in 3 out of the 10 patients. In the 7 remaining patients, artefacts

171 were most frequently located at the apical cap (n=4) and on the anterior wall (n=3)
172 (Fig. S1 in Supplementary Material). The proportion of LV surface affected by
173 artefacts was 9.7% (1.4% – 13.9%) across patients. The median interval between
174 CMR and electrophysiological study was 2 (5 – 23) days, with no relevant clinical
175 events between procedures in any patient (Table 1).

176 Meshes of EAMs were derived from 611 (385 – 1,581) electrode points and were
177 composed of 7,859 (6,880 – 14,952) vertices, of which 59% (48% – 65%) were
178 paired to CMR points (Table 2), with the remaining ones often belonging to non-
179 ventricular structures, or the valve plane or being proximal to CMR artefacts. Pooling
180 data from all cases, the distance between CMR and EAM points was 3.36 (1.64 –
181 5.28) mm. Of all EAM points, 87% and 13% were collected using a Pentaray and a
182 standard ablation catheter, respectively. In 3 cases, intracardiac electrograms were
183 mainly collected with the ablation catheter. In two of these, all points in the EAM
184 meshes had contact force >2 g. In the remaining case, 27% of points in the EAM
185 mesh had either undetermined force or force < 2 g.

186 On CMR, end diastolic and systolic volumes were 248 (197 – 290) mL and 187 (141
187 – 227) mL, respectively. There was a good agreement between the area of the LV
188 (excluding the valve plane) measured from EAM and CMR geometries, with
189 correlation coefficient equal to $r=0.879$ (Supplementary Figure S8). The LV area from
190 EAM was 0.3% (-3.5% – 7.3%) larger than LV area from CMR.

191

192 Correlation between EAM voltage and PSI

193 Comparison between EAM and PSI maps for 2 representative patients, including
194 point-by-point correlations and case-specific ROC curves, is shown in Figure 1 and
195 Figure S2 in Supplementary Material.

196 A significant negative correlation between bipolar voltage and PSI was registered in
197 all patients across all cardiac sites, with a correlation coefficient equal to -0.57 (-0.68,
198 -0.42). PSI correlation with unipolar voltage was also significant, but lower, with
199 correlation coefficient equal to -0.49 (-0.65, -0.36). Correlation between endocardial
200 bipolar voltage and PSI and between endocardial unipolar voltage and PSI was not
201 significantly different across different transmural layers, from endocardial to
202 epicardial PSI layers (Fig. S3 in Supplementary Materials).

203 Agreement in LVZ localization

204 Case by case ROC analyses showed good localization of low-voltage zones (Table
205 2), with AUC for the localization of areas with $V < 1.5$ mV of 0.82 (0.76 – 0.83),
206 sensitivity of 74% (71% – 77%) and specificity of 78% (73% – 83%). Localization of
207 areas with $V < 0.5$ mV was similar (Table 2). The correlation coefficient between the
208 area of low-voltage zones from EAM and PSI maps was 0.87 for $V < 0.5$ mV and 0.79
209 for $V < 1.5$ mV (Figure 2). Agreement between CMR and EAM for localization of LVZ
210 was similar in cases where the majority of data was collected using an ablation
211 catheter (n=3) and where a Pentaray (n=7) catheter was used (Supplementary Table
212 S1).

213 These results were obtained using case-specific ROC-derived PSI thresholds.
214 Similar results were obtained when using a fixed PSI threshold for all cases, taken
215 as the median value of the case-specific PSI thresholds (i.e. $PSI > 41\%$ for $V < 1.5$ mV

216 and $PSI > 46\%$ for $V < 0.5$ mV, Table 2). Sensitivity and specificity were 71% (65%-
217 81%) and 76% (69%-86%) for $V < 1.5$ mV, and 79% (62%-86%) 67% (67%-77%) for
218 $V < 0.5$ mV, respectively.

219 As expected, given that voltage maps were collected on the endocardium, low-
220 voltage zones localization was more accurate using endocardial than epicardial PSI
221 layers (Fig. S4 in Supplementary Material). However, accuracy in low-voltage zones
222 localization using PSI was not significantly different for the sub-endocardial as
223 compared to mid-myocardial layer (Supplementary Fig. S4).

224 Across all patients, mean PSI at ablation sites was 65% (63% – 73%), and 93%
225 (83% – 100%) of ablation sites were located in areas of scar (i.e. above PSI
226 threshold) in PSI maps. The distribution of ablation sites mapped onto a co-
227 registered PSI map, including electrograms recorded at a cardiac site where ablation
228 terminated a subsequently induced VT, is shown for one case in Fig. 4.

229 Choosing a different minimum distance required for pairing CMR and EAM points
230 modified the number of paired sites without significantly affecting the results (Fig. S7
231 in Supplementary Material). Finally, rescaling PSI values to their 5th and 95th
232 percentile value instead of between minimum and maximum did not affect the results
233 (Table 2 in Supplementary Material).

234 [Effect of co-registration misalignments](#)

235 Results of the simulation study to assess low-voltage zones localization after
236 algorithmically altering co-registration showed that misalignments can have a strong
237 impact on the agreement between PSI and voltage, with both PSI-voltage correlation
238 and discrimination of low-voltage zones decreasing for increasing shifts/rotations
239 (Figure 3A). Nevertheless, intra- and inter-operator co-registration variability had little

240 impact on low-voltage zones localization (Figure 3B). The position of the aligned
241 geometries after repeated co-registrations differed by few millimetres (median
242 absolute shift along X, Y and Z axes was equal to 2.6, 2.9 and 2.3 mm, respectively)
243 and degrees (median absolute rotation about X, Y and Z axes was equal to 4.7, 3.1,
244 13.3° respectively) (Supplementary Table 3). Pair-wise correlation coefficients
245 between AUC obtained using reference and additional co-registrations ranged
246 between 0.83 and 0.88, while intraclass correlation coefficients measuring the
247 agreement between AUC estimates across all configurations was equal to 0.86 and
248 0.88 for localization of $V < 1.5$ mV and $V < 0.5$ mV, respectively (Fig. S5 in
249 Supplementary Material).

250 [Effect of spatial smoothing](#)

251 Spatial smoothing gradually improved agreement between voltage and PSI maps.
252 Maximum smoothing (R=6 mm) in both PSI and voltage resulted in an increase in
253 median PSI-voltage correlation coefficient of 13.7% (P=0.002, Figure 3C) and in
254 median AUC of 5.8 (P=0.004, Figure 3C) with respect to non-smoothed maps. Effect
255 of spatial smoothing applied in isolation or in combination to PSI and voltage maps is
256 described in detail in the Supplementary Material (Fig. S6).

257 **Discussion**

258 The aim of this study was to assess performance and limitations of low-voltage
259 zones (LVZ) localisation by optimised LGE-CMR scar imaging in patients with CIEDs
260 and co-registration algorithms for the delineation of scar in patients with CIEDs. We
261 applied state of the art CMR imaging and electro-anatomical mapping to quantify
262 spatial correlation between EAM voltage and PSI across all cardiac sites, focussing
263 on the impact of co-registration and spatial resolution.

264 The main findings are: (1) PSI showed a significant inverse correlation with EAM
265 voltage ($r=-0.57$, interquartile range -0.68 , -0.42) and allowed localization of low-
266 voltage zones with median sensitivity and specificity of 74% and 78%, (2) Small
267 variations in EAM-CMR anatomical co-registration can worsen the localization of
268 low-voltage zones, but the use of the ascending and descending aorta to guide co-
269 registration ensures high intra- and inter-operator reproducibility.

270 With increasing numbers of patients with CIEDs considered for VT ablation due to
271 recurrent arrhythmias and appropriate shocks, techniques are required to improve
272 procedural success rates whilst reducing radiation dose and procedural times. LGE-
273 CMR can aid scar localization and pre-procedural planning (2–7,16), however CMR
274 in patients with CIEDs has generally been avoided due to concerns related to risk
275 and poor image quality from device-related artefact. Few studies had previously
276 investigated EAM and CMR in patients with CIEDs. These had focused on scar size
277 (13), feasibility (17) and correlation between critical sites for re-entry initiation (8),
278 but localization of low-voltage zones by CMR, which is crucial for VT catheter
279 ablation, is still undetermined. This study provides the first assessment of the
280 agreement between voltage and PSI maps in patients with CIEDs. Importantly, it
281 provides quantitative assessment of the impact of co-registration misalignments,
282 which has significant implications particularly in the context of a purely anatomical
283 scar mapping strategy to identify corridors that support re-entry (8,9). Indeed, a
284 recent study has shown that CMR-guided catheter ablation based on localization of
285 critical sites of VT through advance image processing of PSI maps can reduce
286 procedural time and improve outcomes of VT catheter ablation (9). Another potential
287 application for CMR may be in combination with other non-invasive modalities to
288 identify ablation target for stereotactic body radiotherapy (18,19). For instance, ECG-

289 Imaging could be used for identification of VT sites of origin and delineation of the
290 functional electrophysiological substrate related to activation and repolarization
291 abnormalities (14,15,20), whereas CMR could be used for scar delineation and
292 identification of corridors supporting the VT circuit.

293 [Impact of EAM-CMR co-registration](#)

294 Co-registration usually involves minimization of the distance between landmark
295 points, followed by manual adjustment by expert operators. This can introduce bias,
296 particularly if only LV models are used for alignment. We assessed the impact of
297 small random alterations in the co-registration by algorithmically applying rotations
298 and shifts to the EAM after co-registration. We found that these had an impact and
299 that in some cases even small rotations and shifts considerably reduced the
300 agreement between voltage and PSI maps. Despite this, we found that intra and
301 inter-operator co-registration variability was low, and reproducibility of low-voltage
302 zones localization was high (intraclass correlation of AUC equal to 0.86). This is the
303 first study to assess the reproducibility of co-registration, which in this study was
304 optimised by the utilization of the full 3D geometry of the ascending, arch, and
305 descending aorta. The use of the full aortic geometry to co-register CMR and electro-
306 anatomical data was proposed in one of the seminal studies on EAM-CMR
307 integration (21) but has not been adopted as standard clinical practice. Previous
308 studies have used other anatomical landmarks for co-registration, including the
309 position of the mitral annulus, proximal aorta, pulmonary artery, RV or the ostium of
310 the left main coronary artery (4,9) and one study has analysed the effects of rotation
311 (but not shifts) on co-registration accuracy (22).

312 Methodological considerations

313 LGE-CMR correlates well histologically with various models of myocardial fibrosis
314 (23) , but quantitative evaluation of LGE is challenging, with signal thresholding
315 impacting on the projected infarct size. Despite good correlation between EAM
316 voltage and PSI using fixed thresholds based on the median values across the
317 cohort, the optimal PSI threshold varied considerably across cases, and there was a
318 narrow gap between optimum thresholds for localization of low-voltage zones with
319 $V < 1.5$ mV and $V < 0.5$ mV. This highlights the challenge of delineating scar border-
320 zones (0.5 – 1.5 mV), which beyond the limitations of spatial resolution inherent to
321 each modality may be related to the effect of wall thickness (24), catheter
322 configuration (25) , variable CMR contrast kinetics or residual hypersensitivity and
323 signal void related to the presence of the ICD.

324 In primary analysis, we have reported averaged values across CMR layers spanning
325 from sub-endocardium (layer 10%) to mid-myocardium (layer 50%). Layer-by-layer
326 analysis has shown that localization of endocardial low-voltage zones was more
327 accurate when using endocardial layers as compared to epicardial ones
328 (Supplementary Figure S4). However, accuracy in low-voltage zones localization
329 was not significantly different in the sub-endocardial PSI layers as compared to mid-
330 myocardial ones. There are several possible explanations for this, predominantly
331 driven by the limitations of the respective techniques. Whilst mid-myocardial scar
332 may be less apparent on endocardial EAM, there are also challenges in segmenting
333 the true endocardium with CMR and accurately demonstrating the blood-myocardial
334 boundary. The proximity of the 10% layer to the blood pool may occasionally result in
335 partial volume effects within the endocardial voxel which might introduce artefact in
336 the reconstructed 3D model. Despite attempts to limit this by using thin 2D slices

337 (4mm), in some cases this cannot be corrected. This limitation is further accentuated
338 in cases of severe ischaemic cardiomyopathy in view of the reduced wall thickness
339 of infarcted myocardium.

340 Correlation between endocardial unipolar voltage and PSI was similar across all PSI
341 layers, including deeper mid-myocardial and sub-epicardial layer (Supplementary
342 Figure S3). Although endocardial unipolar voltage has been shown to enable
343 localization of epicardial scar, evidence is stronger for non-ischaemic
344 cardiomyopathy and in absence of endocardial scar (26). Furthermore, theoretical
345 (27) and experimental (28) studies have demonstrated that the amplitude of the
346 unipolar electrogram is mainly determined by remote activity (and in particular by the
347 sequence of electrical depolarization) and therefore it is not an ideal parameter for
348 localization of scar.

349 In this study, we used spatial smoothing to reduce noise in both voltage and PSI
350 maps. Spatial smoothing improved agreement between voltage and PSI maps with
351 moderate but significant increase in voltage-PSI correlation and low-voltage zone
352 discrimination. However, since smoothing reduces spatial resolution, its use may be
353 limited to the localization of large areas of scar as opposed to the fine details of the
354 scar architecture.

355 **Limitations**

356 Our study is limited by the small sample size. However, patients had high-density
357 EAM and complete geometry of the aorta, which is crucial to ensure detailed
358 delineation of the substrate and optimal co-registration. EAM was used as a
359 reference for the identification of abnormal tissue, and although Pentaray was used
360 to collect most points, an ablation catheter was occasionally used. Bipolar voltage

361 can be affected by wave-front directionality and catheter configuration (25).
362 Although higher spatial resolution LGE imaging can be obtained using 3D MRI
363 (1.9×1.9×1.9 mm³), 3D wideband LGE imaging is generally unfeasible in patients
364 with frequent ventricular arrhythmias awaiting ablation. Finally, this study was limited
365 to endocardial maps and did not focus on the utility of integrating CMR with EAM
366 data during catheter ablations (6–8). This however should be the focus of further
367 investigation.

368 **Conclusions**

369 In patients with CIEDs, use of novel wideband CMR LGE sequences and strategies
370 to optimize co-registration can localize areas of scar with good accuracy. To fully
371 establish the role of CMR in assisting VT ablation, effort should be focused on
372 standardising co-registration, improving data acquisition and reducing noise in both
373 modalities.

374 **Perspectives**

375 *Competency in medical knowledge:* This study shows that optimised cardiac MRI
376 enables non-invasive localization of scar in patients with cardiac implantable
377 electronic devices and it highlights the importance of using the thoracic aorta as a
378 landmark for accurate co-registration with electro-anatomical maps.

379 *Translational outlook:* Optimised MRI sequences and accurate co-registration of
380 cardiac MRI scar maps with electro-anatomical geometries could improve VT
381 ablation.

382

383

384 **References**

- 385 1. Graham AJ., Orini M., Lambiase PD. Limitations and challenges in mapping
386 ventricular tachycardia: New technologies and future directions. *Arrhythmia*
387 *Electrophysiol Rev* 2017;6(3):118–24. Doi: 10.15420/aer.2017.20.1.
- 388 2. Ashikaga H., Sasano T., Dong J., et al. Magnetic resonance-based anatomical
389 analysis of scar-related ventricular tachycardia: Implications for catheter
390 ablation. *Circ Res* 2007;101(9):939–47. Doi:
391 10.1161/CIRCRESAHA.107.158980.
- 392 3. Codreanu A., Odille F., Aliot E., et al. Electroanatomic Characterization of
393 Post-Infarct Scars: Comparison With 3-Dimensional Myocardial Scar
394 Reconstruction Based on Magnetic Resonance Imaging. *J Am Coll Cardiol*
395 2008;52(10):839–42. Doi: 10.1016/J.JACC.2008.05.038.
- 396 4. Wijnmaalen AP., Van Der Geest RJ., Van Huls Van Taxis CFB., et al. Head-to-
397 head comparison of contrast-enhanced magnetic resonance imaging and
398 electroanatomical voltage mapping to assess post-infarct scar characteristics
399 in patients with ventricular tachycardias: Real-time image integration and
400 reversed registration. *Eur Heart J* 2011;32(1):104–14. Doi:
401 10.1093/eurheartj/ehq345.
- 402 5. Sramko M., Hoogendoorn JC., Glashan CA., Zeppenfeld K. Advancement in
403 cardiac imaging for treatment of ventricular arrhythmias in structural heart
404 disease. *Europace* 2019;21(3):383–403. Doi: 10.1093/europace/euy150.
- 405 6. Andreu D., Berruezo A., Ortiz-Pérez JT., et al. Integration of 3D
406 electroanatomic maps and magnetic resonance scar characterization into the
407 navigation system to guide ventricular tachycardia ablation. *Circ Arrhythmia*

- 408 Electrophysiol 2011;4(5):674–83. Doi: 10.1161/CIRCEP.111.961946.
- 409 7. Andreu D., Penela D., Acosta J., et al. Cardiac magnetic resonance–aided
410 scar dechanneling: Influence on acute and long-term outcomes. *Heart Rhythm*
411 2017;14(8):1121–8. Doi: 10.1016/j.hrthm.2017.05.018.
- 412 8. Roca-Luque I., Van Breukelen A., Alarcon F., et al. Ventricular scar channel
413 entrances identified by new wideband cardiac magnetic resonance sequence
414 to guide ventricular tachycardia ablation in patients with cardiac defibrillators.
415 *Europace* 2020;22(4):598–606. Doi: 10.1093/europace/euaa021.
- 416 9. Soto-Iglesias D., Penela D., Jáuregui B., et al. Cardiac Magnetic Resonance-
417 Guided Ventricular Tachycardia Substrate Ablation. *JACC Clin Electrophysiol*
418 2020;6(4):436–47. Doi: 10.1016/j.jacep.2019.11.004.
- 419 10. Bhuva AN., Kellman P., Graham A., et al. Clinical impact of cardiovascular
420 magnetic resonance with optimized myocardial scar detection in patients with
421 cardiac implantable devices. *Int J Cardiol* 2019;279:72–8. Doi:
422 10.1016/j.ijcard.2019.01.005.
- 423 11. Seewöster T., Löbe S., Hilbert S., et al. Cardiovascular magnetic resonance
424 imaging in patients with cardiac implantable electronic devices: best practice
425 and real-world experience. *Europace* 2019;21(8):1220–8. Doi:
426 10.1093/europace/euz112.
- 427 12. Dickfeld T., Tian J., Ahmad G., et al. MRI-guided ventricular tachycardia
428 ablation integration of late gadolinium-enhanced 3D scar in patients with
429 implantable cardioverter- defibrillators. *Circ Arrhythmia Electrophysiol*
430 2011;4(2):172–84. Doi: 10.1161/CIRCEP.110.958744.

- 431 13. Stevens SM., Tung R., Rashid S., et al. Device artifact reduction for magnetic
432 resonance imaging of patients with implantable cardioverter-defibrillators and
433 ventricular tachycardia: Late gadolinium enhancement correlation with
434 electroanatomic mapping. *Heart Rhythm* 2014;11(2):289–98. Doi:
435 10.1016/j.hrthm.2013.10.032.
- 436 14. Graham AJ., Orini M., Zacur E., et al. Simultaneous Comparison of
437 Electrocardiographic Imaging and Epicardial Contact Mapping in Structural
438 Heart Disease. *Circ Arrhythmia Electrophysiol* 2019;12(4):e007120. Doi:
439 10.1161/CIRCEP.118.007120.
- 440 15. Graham AJ., Orini M., Zacur E., et al. Evaluation of ECG Imaging to Map
441 Haemodynamically Stable and Unstable Ventricular Arrhythmias. *Circ*
442 *Arrhythmia Electrophysiol* 2020. Doi: 10.1161/circep.119.007377.
- 443 16. Desjardins B., Crawford T., Good E., et al. Infarct architecture and
444 characteristics on delayed enhanced magnetic resonance imaging and
445 electroanatomic mapping in patients with postinfarction ventricular arrhythmia.
446 *Heart Rhythm* 2009;6(5):644–51. Doi: 10.1016/j.hrthm.2009.02.018.
- 447 17. Singh A., Kawaji K., Goyal N., et al. Feasibility of Cardiac Magnetic Resonance
448 Wideband Protocol in Patients With Implantable Cardioverter Defibrillators and
449 Its Utility for Defining Scar. *Am J Cardiol* 2019;123(8):1329–35. Doi:
450 10.1016/j.amjcard.2019.01.018.
- 451 18. Robinson CG., Samson PP., Moore KMS., et al. Phase I/II Trial of
452 Electrophysiology-Guided Noninvasive Cardiac Radioablation for Ventricular
453 Tachycardia. *Circulation* 2019;139(3):313–21. Doi:
454 10.1161/CIRCULATIONAHA.118.038261.

- 455 19. Cuculich PS., Schill MR., Kashani R., et al. Noninvasive Cardiac Radiation for
456 Ablation of Ventricular Tachycardia. *N Engl J Med* 2017;377(24):2325–36. Doi:
457 10.1056/nejmoa1613773.
- 458 20. Wang Y., Cuculich PS., Zhang J., et al. Noninvasive Electroanatomic Mapping
459 of Human Ventricular Arrhythmias with Electrocardiographic Imaging. *Sci*
460 *Transl Med* 2011;3(98):98ra84-98ra84. Doi: 10.1126/scitranslmed.3002152.
- 461 21. Reddy VY., Malchano ZJ., Holmvang G., et al. Integration of cardiac magnetic
462 resonance imaging with three-dimensional electroanatomic mapping to guide
463 left ventricular catheter manipulation: Feasibility in a porcine model of healed
464 myocardial infarction. *J Am Coll Cardiol* 2004;44(11):2202–13. Doi:
465 10.1016/j.jacc.2004.08.063.
- 466 22. Tao Q., Milles J., Van Huls Van Taxis C., et al. Toward magnetic resonance-
467 guided electroanatomical voltage mapping for catheter ablation of scar-related
468 ventricular tachycardia: A comparison of registration methods. *J Cardiovasc*
469 *Electrophysiol* 2012;23(1):74–80. Doi: 10.1111/j.1540-8167.2011.02167.x.
- 470 23. Iles LM., Ellims AH., Llewellyn H., et al. Histological validation of cardiac
471 magnetic resonance analysis of regional and diffuse interstitial myocardial
472 fibrosis. *Eur Heart J Cardiovasc Imaging* 2015;16(1):14–22. Doi:
473 10.1093/ehjci/jeu182.
- 474 24. Glashan CA., Androulakis AFA., Tao Q., et al. Whole human heart histology to
475 validate electroanatomical voltage mapping in patients with non-ischaemic
476 cardiomyopathy and ventricular tachycardia. *Eur Heart J* 2018;39(31):2867–
477 75. Doi: 10.1093/eurheartj/ehy168.
- 478 25. Takigawa M., Relan J., Kitamura T., et al. Impact of Spacing and Orientation

479 on the Scar Threshold With a High-Density Grid Catheter. *Circ Arrhythmia*
480 *Electrophysiol* 2019;12(9):e007158. Doi: 10.1161/CIRCEP.119.007158.

481 26. Hutchinson MD., Gerstenfeld EP., Desjardins B., et al. Endocardial unipolar
482 voltage mapping to detect epicardial ventricular tachycardia substrate in
483 patients with nonischemic left ventricular cardiomyopathy. *Circ Arrhythmia*
484 *Electrophysiol* 2011;4(1):49–55. Doi: 10.1161/CIRCEP.110.959957.

485 27. Potse M., Vinet A., Opthof T., Coronel R. Validation of a simple model for the
486 morphology of the T wave in unipolar electrograms. *Am J Physiol Heart Circ*
487 *Physiol* 2009;297(2):H792–801. Doi: 10.1152/ajpheart.00064.2009.

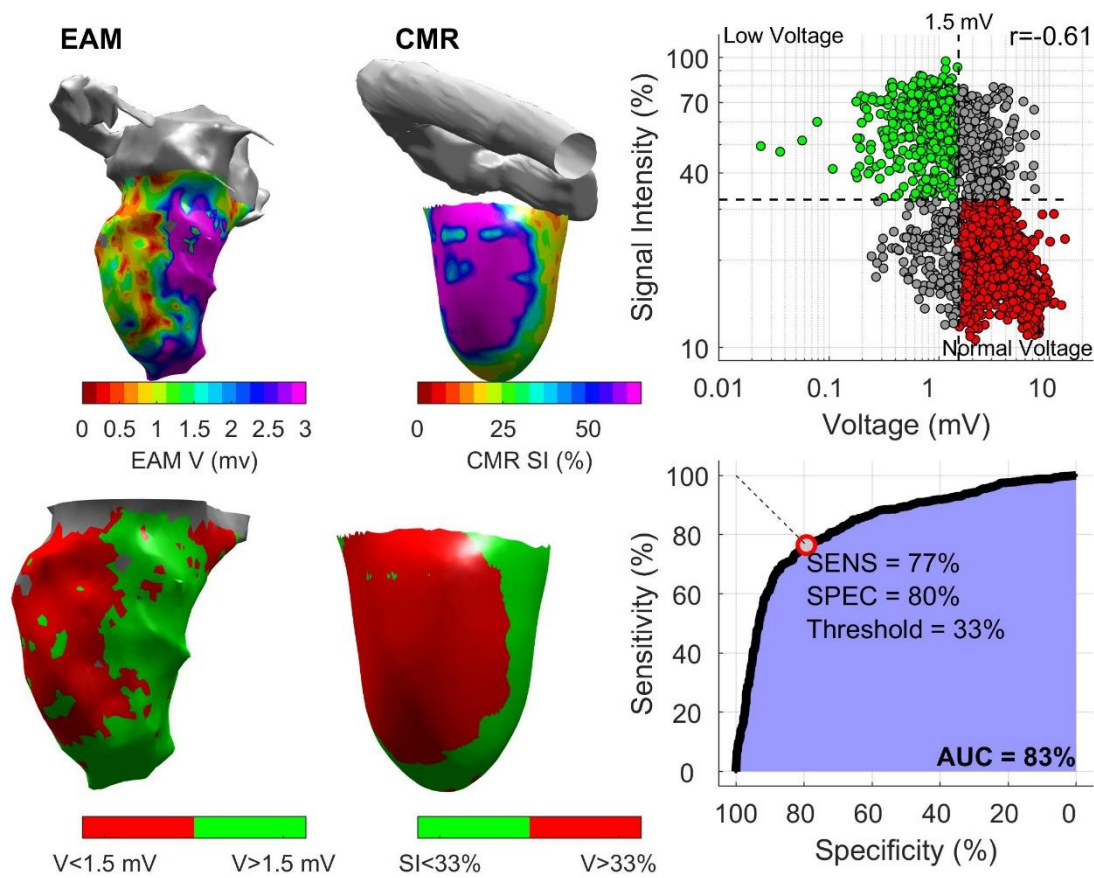
488 28. Orini M., Taggart P., Lambiase PD. In vivo human sock-mapping validation of
489 a simple model that explains unipolar electrogram morphology in relation to
490 conduction-repolarization dynamics. *J Cardiovasc Electrophysiol*
491 2018;29(7):990–7. Doi: 10.1111/jce.13606.

492

493

494 **Figures**

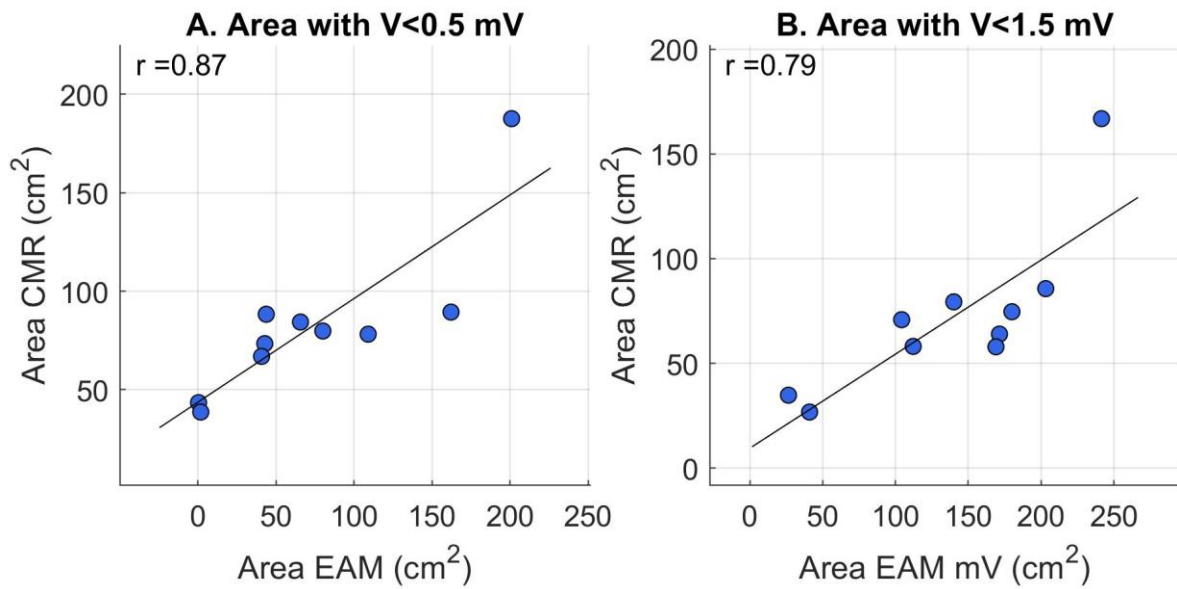
495 **Figure 1.**



496

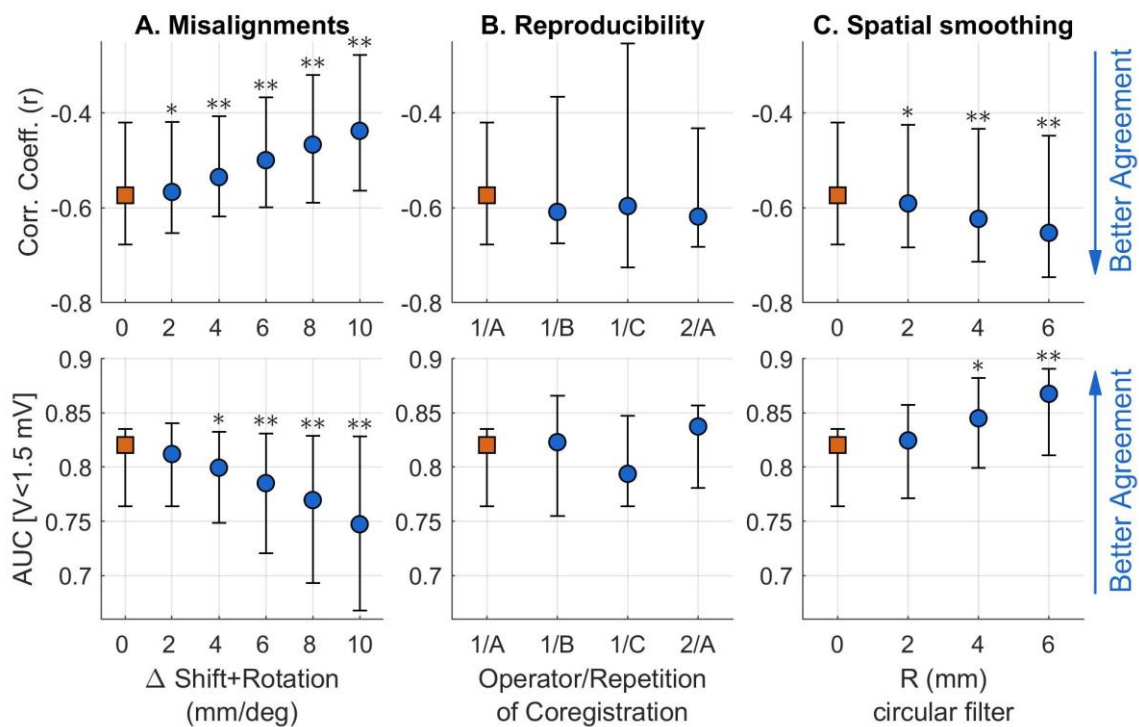
497 **Figure 1:** Comparison between EAM and LGE-CMR (example Subject #9). Top:
498 voltage and CMR-intensity maps (30 transmural) shown side-by-side. Bottom:
499 Low-voltage areas ($V < 1.5$ mV) and areas with $PSI > 33\%$ indicating abnormal tissue
500 are shown on the left and right, respectively. Maps from left to right are shown in the
501 same reference system. Top-right inset shows correlation between voltage and PSI
502 (on loglog scale), with green representing true positives and red representing true
503 negative. Correlation coefficient was $r = -0.61$. Bottom-right inset shows ROC curve
504 with a circle representing optimal threshold for identification of low-voltage zones.
505 EAM: Electroanatomical map. LGE-CMR: Late gadolinium enhancement
506 cardiovascular magnetic resonance. AUC: Area under the ROC curve.

507 Figure 2.



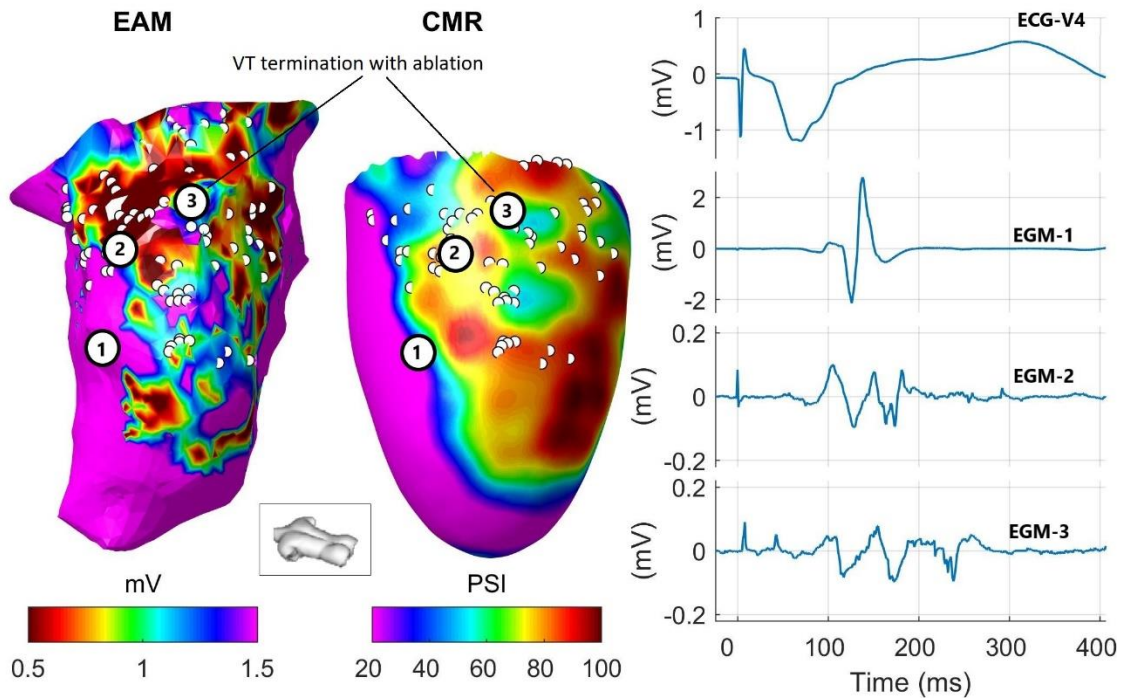
508

509 **Figure 2:** Correlation across all subjects between scar area measured using EAM
510 and CMR-LGE automated scar segmentation. Linear fitting is reported with a solid
511 line and correlation coefficient (r) is shown on the top-left corner. On EAM, low-
512 voltage zones were defined with V < 0.5 mV and V < 1.5 mV. On CMR maps, areas
513 representing low-voltage zones were identified with case-specific thresholds
514 obtained through ROC analysis (average of layers spanning from sub-endocardium,
515 layer 10, to mid-myocardium, layer 50).



517

518 **Figure 3:** Effect of misalignment in co-registration (A), inter- and intra-operator
 519 variability of co-registration (B) and spatial smoothing of voltage and pixel intensity
 520 signal (PSI) maps (C) on EAM-CMR agreement. A: Expert-based co-registration of
 521 each case was algorithmically modified by simultaneously shifting (Δ mm) and
 522 rotating (Δ deg) the voltage map along and across the 3 orthogonal axes (64 iteration
 523 per Δ and patient). B: EAM and voltage maps were co-registered by a first operator
 524 three times (1A, 1B and 1C) and by a second operator (2A). C: Increasing degree of
 525 spatial smoothing of voltage and PSI maps using a circular filter of radius equal to 2,
 526 4 and 6 mm. Markers and whiskers represent median value and interquartile range.
 527 r: Spearman's correlation coefficient between PSI and voltage across cardiac sites.
 528 AUC: Area under the ROC curve for localization of zones with $V < 1.5$ mV. * $P < 0.05$;
 529 ** $P < 0.005$ (Wilcoxon signed-rank test) with respect to reference values (red
 530 squares, corresponding to $\Delta = 0$ in A; 1A in B; $R = 0$ in C).



532

533 **Figure 4:** Left: Electro-anatomical map (EAM) collected while pacing from the RV
 534 apex and CMR pixel signal intensity (PSI) map (endocardial layer corresponding to
 535 10% of wall thickness). White dots indicate ablation sites projected onto the two
 536 geometries. Electrograms (EGM) from sites labelled 1 (healthy tissue), 2 (dense
 537 scar) and 3 (VT exit site) are shown on the right as EGM-1,2 and 3. Ablation
 538 proximal to site 3 terminated ventricular tachycardia induced after substrate
 539 mapping. Note y-scale is adjusted to the signal's amplitude.

540

541 **Tables**

542 **Table 1**

ID	Sex (M/F)	Age (years)	Aetiology	Type of Device	MR Conditional	LVEF (%)	Artefacts (% of myocardium)	Interval CMR-ablation (weeks)	First/ Redo Ablation
1	M	68	IHD	CRTD	No	52	13.9	0.3	First
2	M	69	IHD	ICD	Yes	34	1.4	44.3	First
3	M	79	IHD	CRTD	No	16	0.0	0.9	Redo
4	M	84	IHD	ICD	No	19	9.7	4.0	First
5	F	79	IHD	ICD	Yes	20	9.8	0.6	First
6	M	84	IHD	ICD	No	25	10.2	0.0	First
7	M	78	IHD	CRTD	Yes	10	8.8	0.0	Redo
8	M	56	DCM	CRTD	No	20	28.9	0.3	First
9	M	73	IHD	ICD	Yes	41	0.2	8.3	First
10	M	72	IHD	CRTD	Yes	23	25.9	1.0	First

543

544 **Table 1: Baseline demographics, clinical and CMR data of the patient cohort.**

545 CMR-EP interval: time delay between CMR and VT ablation.

546

547 Table 2

Patient number	Points		Corr. Coeff.	V<0.5 mV					V<1.5 mV				
	EAM Mesh	Paired (%)		PREV (%)	AUC	THR (%)	SENS (%)	SPEC (%)	PREV (%)	AUC (%)	THR (%)	SENS (%)	SPEC (%)
1	3,871	58	-0.54	1	-	-	-	-	22	0.76	50	74	71
2	22,669	83	-0.32	22	0.58	35	64	54	55	0.70	33	68	67
3	7,947	48	-0.68	35	0.87	46	83	77	63	0.83	42	73	79
4	7,770	43	-0.69	22	0.83	50	83	72	62	0.87	41	78	83
5	6,880	65	-0.42	30	0.77	51	80	72	56	0.69	47	64	73
6	14,952	55	-0.50	49	0.80	41	72	76	76	0.81	37	71	78
7	15,583	41	-0.73	54	0.91	53	85	87	72	0.87	46	76	86
8	8,896	61	-0.61	22	0.79	49	78	69	44	0.83	44	80	76
9	2,438	88	-0.61	5	0.75	38	81	66	36	0.83	33	77	80
10	7,674	60	-0.31	80	0.69	36	77	60	96	0.79	33	75	84
Median	7,859	59	-0.57	26	0.79	46	80	72	59	0.82	41	74	78
Q1	6,880	48	-0.68	22	0.73	37	76	65	44	0.76	33	71	73
Q3	14,952	65	-0.42	49	0.84	51	83	76	72	0.83	46	77	83

548

549 **Table 2:** Low-voltage zone localization. EAM: Electroanatomical map. MED: Median.

550 Q1 and Q3: First and third quartile, respectively. PREV: Prevalence of LVZ across

551 paired points. AUC: Area under the ROC curve. THR: PSI Case-specific threshold.

552 SENS: Sensitivity. SPEC: Specificity.